

The stratorotational instability of Taylor-Couette flows with moderate Reynolds numbers

G. Rüdiger¹, T. Seelig², M. Schultz¹, M. Gellert¹, Ch. Egbers²,
U. Harlander²

¹Leibniz-Institut für Astrophysik Potsdam, An der Sternwarte 16, D-14467 Potsdam, Germany

²Aerodynamik und Strömungslehre, BTU Cottbus-Senftenberg, Siemens-Halske-Ring 14, D-03046 Cottbus, Germany

E-mail: uwe.harlander@b-tu.de

Abstract. In view of new experimental data the instability against adiabatic nonaxisymmetric perturbations of a Taylor-Couette flow with an axial density stratification is considered in dependence of the Reynolds number (Re) of rotation and the Brunt-Väisälä number (Rn) of the stratification. The flows at and beyond the Rayleigh limit become unstable between a lower and an upper Reynolds number (for fixed Rn). The rotation can thus be too slow or too fast for the stratorotational instability. The upper Reynolds number above which the instability decays, has its maximum value for the potential flow (driven by cylinders rotating according to the Rayleigh limit) and decreases strongly for flatter rotation profiles finally leaving only isolated islands of instability in the (Rn/Re) map. The maximal possible rotation ratio μ_{\max} only slightly exceeds the shear value of the quasi-uniform flow with $U_\phi \simeq \text{const}$.

Along and between the lines of neutral stability the wave numbers of the instability patterns for all rotation laws beyond the Rayleigh limit are mainly determined by the Froude number Fr which is defined by the ratio between Re and Rn . The cells are highly prolate for $Fr > 1$ so that measurements for too high Reynolds numbers become difficult for axially bounded containers. The instability patterns migrate azimuthally slightly faster than the outer cylinder rotates.

1. Introduction

The magnetorotational instability is now commonly invoked in order to understand the origin of the turbulence in accretion disks. This is also because no purely hydrodynamic linear instability exists in accretion disks rotating with the Kepler law $\Omega \propto R^{-3/2}$. A linear instability is possible, however, when an axial shear $\Omega = \Omega(z)$ is included. In accordance with the stability condition

$$\frac{1}{R^4} \frac{\partial}{\partial R} (R^4 \Omega^2) > \frac{k_R}{k_z} \frac{\partial \Omega^2}{\partial z} \quad (1)$$

[32, here written in cylindric coordinates (R, ϕ, z) and in terms of the Boussinesq approximation] the flow could be unstable for axisymmetric perturbations with suitable wave numbers \mathbf{k} . For weak vertical shear the wave numbers of the possible instability pattern must fulfill the condition $k_R \gg k_z$ resulting in cells strongly aligned to the rotation axis. The growth time of this vertical-shear instability, however, proves to be longer than the rotation time by more than one order of magnitude [1]. The vertical-shear instability which is closely related to the Goldreich-Schubert-Fricke instability [11, 9] also has been considered when the axial shear is accompanied by an axial density stratification [19, 26, 21] resulting in higher growth rates despite of the stabilizing action of the axial entropy gradient. It is obvious that the thermal behavior of the material will play an important role as adiabatic perturbations are much stronger suppressed by the restoring buoyancy than those with an effective heat transport [31].

Such purely hydrodynamic instabilities are of particular interest for cool protostellar disks where the electric conductivity is so low that magnetic effects should be unimportant. Another possibility for a hydrodynamic instability is the nonlinear shear instability [6, 29]. However, a final solution of this problem with numerical simulations remains difficult because of the large Reynolds numbers required. The more simple question is whether the direct combination of radial shear *and* the axial stratification for themselves are stable. This, however, is hard to imagine on the basis of the Solberg-Høiland conditions

$$\frac{1}{R^3} \frac{\partial(R^4 \Omega^2)}{\partial R} - \frac{1}{C_p \rho} \frac{\partial P}{\partial z} \frac{\partial S}{\partial z} > 0 \quad (2)$$

and

$$\frac{\partial P}{\partial z} \left(\frac{\partial(R^4 \Omega^2)}{\partial R} \frac{\partial S}{\partial z} - \frac{\partial(R^4 \Omega^2)}{\partial z} \frac{\partial S}{\partial R} \right) < 0 \quad (3)$$

necessary for stability of compressible material. Here P is the pressure, C_p the heat capacity for constant pressure and S the specific entropy. Equation (2) provides both the Rayleigh condition for stability, $\partial(R^4 \Omega^2)/\partial R > 0$, for isentropic axial stratification and the Schwarzschild criterion for stability, $\partial S/\partial z > 0$, for resting fluids. If, however, a fluid with $\partial P/\partial z < 0$ rotates with a stable rotation law $\Omega = \Omega(R)$, then also the second stability Solberg-Høiland condition (3) is fulfilled with the Schwarzschild criterion

$$\frac{\partial S}{\partial z} > 0 \quad (4)$$

[17, 8]. A combination of stable axial density stratifications and centrifugally-stable rotation laws should thus also be stable. Note, however, that Eqs. (2) and (3) are only valid for stability against axisymmetric perturbations within the short-wave approximation [28].

The stabilizing role of axial density stratification has indeed been observed in several Taylor-Couette experiments with stationary outer cylinder and for incompressible fluids [4, 12, 5]. The axial density stratification increases the critical Reynolds numbers (of

the inner cylinder) for the onset of the axisymmetric mode. With numerical simulations [12] found the first unstable mode indeed to be axisymmetric if the Prandtl number has been chosen high enough. One can show that the excitation of this mode needs increasingly higher Reynolds numbers if also the outer cylinder rotates so that it goes to infinity if $\Omega \propto 1/R^2$ is approached [25]. This rotation law is curl-free ($\text{curl} \mathbf{U} = 0$, called the ‘potential’ flow) and separates the centrifugally unstable flows from the stable flows defining the Rayleigh limit. These findings are in agreement with the criterion (4). However, under the presence of an axial density stratification persisting *nonaxisymmetric disturbances* for the stable flows slightly beyond the Rayleigh limit have been observed [33]. Numerical studies also revealed that the combination of convective-stable axial density stratification and centrifugally-stable differential rotation is linearly unstable against nonaxisymmetric perturbations [18, 34, 25, 30]. Obviously, the criteria (2) and (3) are only necessary for stability but not sufficient. This instability against nonaxisymmetric modes (now called the stratorotational instability, SRI) does not require the presence of radial boundaries [7].

Almost all previous calculations concerned Boussinesq fluids (with infinite speed of sound) fulfilling the incompressibility condition $\text{div} \mathbf{U} = 0$ (see, however [30]). The density fluctuations are assumed as due to the action of fluctuating flows within a medium of axially stratified background density. A possible molecular density diffusion κ is often ignored in the calculations because of its smallness leading to Schmidt numbers exceeding $\mathcal{O}(10^2)$ [12, 5, 16]. For too small Schmidt number the diffusion suppresses density perturbations. Following [12] we shall use in this paper the notation Prandtl number for the ratio of viscosity ν and density-diffusivity ν/κ instead of Schmidt number because of its identical definition if a temperature stratification is used instead of the density stratification.

The *inviscid* equations of [34] for the potential flow combining a rigid inner boundary with an infinite gap width have been solved showing that the most unstable modes belong to high azimuthal wave numbers [15]. Weak stratification suppresses the instability. Pure Keplerian rotation – which is not an exact solution of the zero-order equations – proves to be stable for disturbances with azimuthal mode number smaller than 14. The same system of inviscid equations is also reported as allowing instability if the angular velocity of the rotation increases outwards (‘superrotation’, see [20]). Taylor-Couette flows with *finite viscosity* have been considered even formulating a stability criterion [25]. For a medium gap and a fixed small Froude number of 0.5 the flattest unstable rotation law was $\Omega \propto 1/R$ which has experimentally been confirmed by [14]. Later calculations demonstrated that for unity Froude number indeed $\Omega \propto 1/R$ approaches the smoothest unstable rotation law for a wide variation of the gap widths [23]. [13] reported new experimental results with a small-gap container with variable rotation laws including the existence of minimal and maximal values of the Reynolds number between them the SRI exists. We shall here discuss several of their findings in the light of new experimental data and theoretical results also considering the critical

Reynolds number for fixed density stratification as a function of the ratio

$$\mu = \frac{\Omega_{\text{out}}}{\Omega_{\text{in}}} \quad (5)$$

of the rotation rates of the outer and the inner cylinder.

The paper is organized as follows. In Section 2 we briefly describe the experimental setup and in Section 3 details about the Taylor-Couette flow are given model that is linearized and solved numerically. This is done first in Section 4 where we present stability properties for the most prominent example of potential flow (‘the Rayleigh limit’). Subsequently, in Section 5 we do the same for flat rotation laws and compare stability diagrams and drift rates with the ones obtained from experimental measurements. Moreover, in Section 6 we discuss the axial wave number of the unstable modes and give limits for the Froude number in view of the finite size of the experimental apparatus. In Section 7 the growth rate of the instability is shortly commented.

2. Experimental realization

The SRI experiment of the BTU Cottbus-Senftenberg is used to probe the main results of the presented stability analysis. In opposition to earlier experiments it works with a stable stratification due to a positive axial temperature gradient dT/dz by heating the cylindrical gap from *above*, see [10]. Instead of the density gradient it is here the temperature gradient that defines the Brunt-Väisälä frequency. Beyond the Rayleigh limit a destabilization happens already for a temperature difference between top and bottom of a few K. The container has an aspect ratio of $\Gamma = H/(R_{\text{out}} - R_{\text{in}}) = 10$ and a ratio

$$\eta = \frac{R_{\text{in}}}{R_{\text{out}}} \quad (6)$$

of the two cylinder radii R_{in} and R_{out} of $\eta = 0.52$ (Fig. 1). By the rotation the instability cells become axially elongated. We shall show that an aspect ratio of only $\Gamma = 10$ does not allow too fast rotation. The outer cylinder is made of acrylic glass and accessible for Particle Image Velocimetry (PIV). The inner cylinder is made of anodized aluminum in order to suppress disturbing optical reflection. Both horizontal endplates are connected to the outer cylinder.

On the upper endplate 12 Peltier elements have been installed. Six of them operate as heat source and were mounted in hexagonal order at the inner part of the plate. All further Peltier elements work as cooling system. They are mounted on top of aluminum blocks. Water is cooled inside the aluminum blocks and continuously pumped downward into a reservoir mounted below the bottom aluminum endplate to cool the endplate and keep its temperature constant. The inner and outer cylinders are driven independently by two DC motor units. The axial temperature profile is analyzed with an infrared camera. Flow velocity measurements are done with a corotating mini-PIV system with a green laser module and a corotating camera. The tank is filled with silicone oil M5 with $Pr = 57$. Figure 1 shows the position and extension of the PIV section 34.5cm

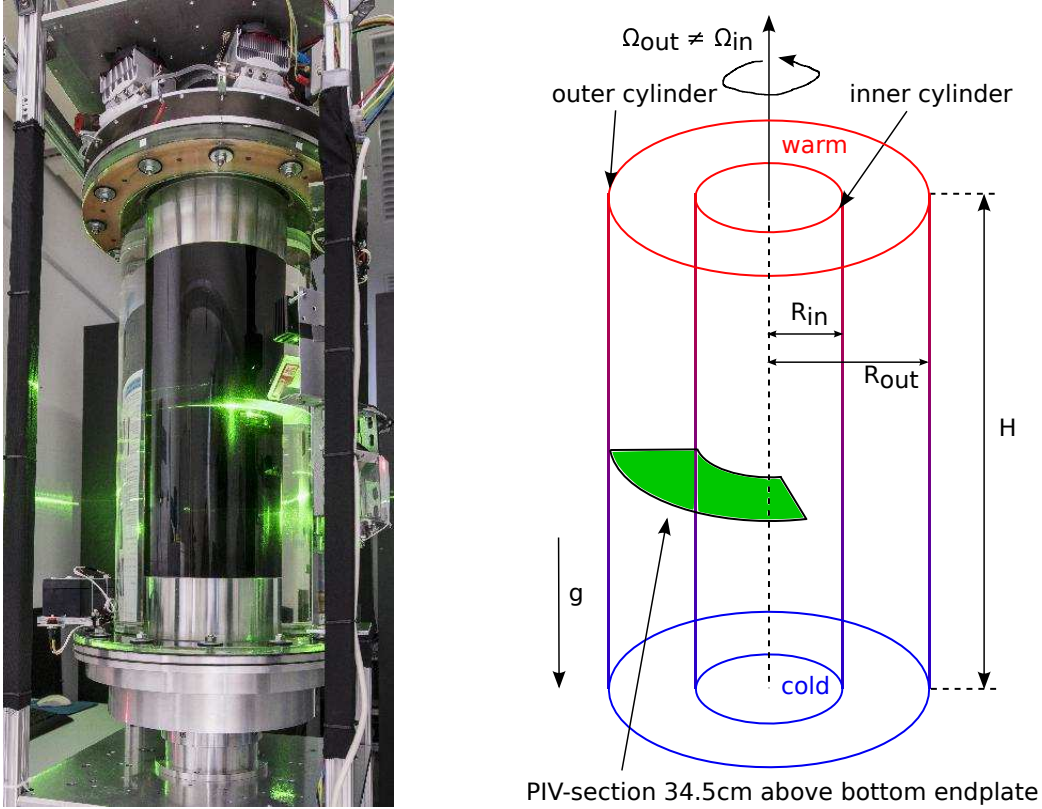


Figure 1. Left: The SRI experiment at the Brandenburgische Technische Universität Cottbus-Senftenberg. The temperature difference between top and bottom varies from 1 to 5 K. Right: Sketch of the experimental cell and position of the PIV-section used to determine the flow state and the drift rate. It is $R_{in} = 7.5$ cm, $R_{out} = 14.5$ cm. $H = 70$ cm, $\eta = 0.52$.

above the cooled bottom endplate. We calibrated the PIV section with a chess board pattern. Velocity fields are computed by the use of MatPIV [27]. Initially, the velocity components are given in Cartesian coordinates. The origin of the PIV segment, needed for polar coordinate transformations, is determined by applying the calibration grid. In a next step the grid and velocity components have been transformed into polar coordinates. On a line of constant angle and varying radial gridpoints ($\phi = 0$, central part of the PIV-section) we stored the polar velocity components as time series. We next compute power spectra for each set of PIV data. Transition from a stable to an unstable flow is signaled by the occurrence of isolated peaks in the spectra. In a subsequent step we reconstruct the SRI modes by applying a least-square harmonic fit to the PIV time series using the peak frequencies of the power spectra. In that way we obtain the spatial structure of the modes (the azimuthal wave numbers) and their development in time (the azimuthal drift rates of the patterns). Figure 2 shows a SRI velocity field $\mathbf{u} = (u_R, \Delta u_\phi = u_\phi - \bar{u}_\phi^t(R))^T$ in the azimuthal-radial plane measured with the PIV. The magnitude $|\mathbf{u}| = (u_R^2 + \Delta u_\phi^2)^{1/2}$ is shown in red if Δu_ϕ is positive (prograde) and in blue if Δu_ϕ is negative (retrograde). The pattern will be decomposed

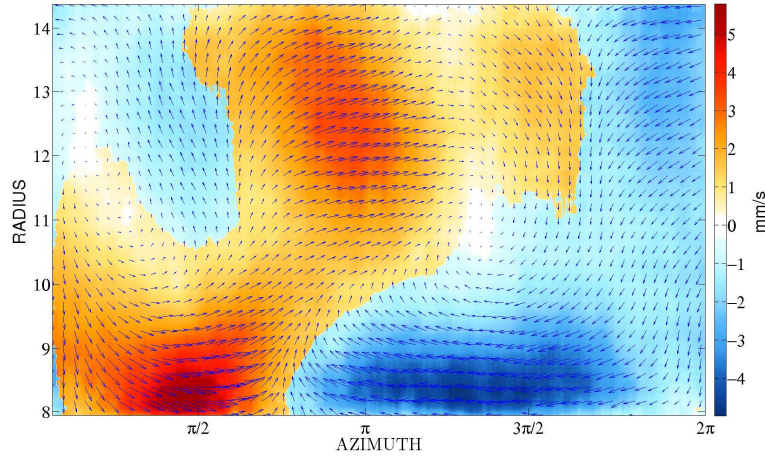


Figure 2. Timeseries associated with the period/azimuth of mode $m = 1$ of the nonaxisymmetric PIV velocity field in the (R/ϕ) plane with dominating $m = 1$ mode and one cell in radius. Note the azimuthal phase shift of the maxima indicating the existence of two vortices shifted in azimuth by 180° . A harmonic reconstruction with single peak frequencies provides the energy of the modes with various m . The whole pattern drifts in the direction of increasing azimuth. $\mu = 0.45$, $Re = 406$, $Rn = 206$.

into single modes with different azimuthal wave numbers from which the azimuthal drift of each single mode can be derived. More details about the experiment and the data analysis are given by [24].

Taylor-Couette systems with endplates generate strong shear layers. The resulting meridional circulation modifies the rotation profile close to the endplates. For strong enough differential rotation this shear layers become unstable and nonaxisymmetric modes develop [3, 2]. Adding stratification suppresses this instability and reduces the shear layer and the related circulations [16]. Both effects might appear in the experiment and it is difficult to say how strong the stratification must be in order to stabilize the shear-layer instability. We therefore probed the stability of *unstratified* flows beyond the Rayleigh limit which all should be stable against axisymmetric and nonaxisymmetric perturbations. The results are shown in Fig. 3 in comparison with nonlinear numerical simulations by [10]. The unstable flows in the experiment are found above the line that marks the onset of the shear-layer instability in simulations. The critical Reynolds numbers for flows near the Rayleigh limit are rather low (of order 10^3) so that only experiments with flatter rotation laws appear to be reasonable.

3. The Taylor-Couette flow model

We have to formulate the basic state with prescribed velocity profile $\mathbf{U} = (0, R\Omega, 0)$, given rotation law $\Omega = \Omega(R)$ and density axial stratification $\rho_0(z)$. The equations for the background density and azimuthal flow profile are

$$\frac{U_\phi^2}{R} = \frac{1}{\rho_0} \frac{\partial P}{\partial R}, \quad \frac{1}{\rho_0} \frac{\partial P}{\partial z} = -g, \quad \frac{\partial^2 U_\phi}{\partial R^2} + \frac{1}{R} \frac{\partial U_\phi}{\partial R} - \frac{U_\phi}{R^2} = 0. \quad (7)$$

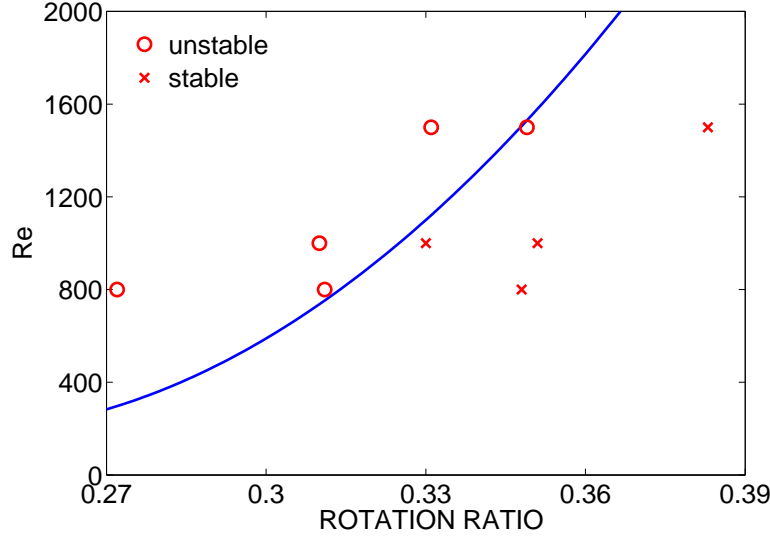


Figure 3. Re versus μ for Taylor-Couette experiments without stratification. The endplate effects lead to a nonaxisymmetric instability pattern (red circles) due to the shear-layer instability. All crosses representing stability are located right of the theoretical curve while the circles are located at the curve or left of it. Close to the Rayleigh limit at $\mu = 0.27$ this instability appears already for low Reynolds numbers. Numerical simulations with (!) endplates provide the solid blue line.

The last equation yields

$$\Omega = a + \frac{b}{R^2} \quad (8)$$

as the solution for the angular velocity where a and b are free constants. The last term in (8) is curl-free (the ‘potential’ flow) defining the Rayleigh limit in the theory of the Taylor-Couette flows. The two free constants must be fixed by the boundary values Ω_{in} and Ω_{out} of the angular velocity of the inner cylinder (radius R_{in}) and the outer cylinder (radius R_{out}). It follows

$$a = \Omega_{\text{in}} \frac{\mu - \eta^2}{1 - \eta^2}, \quad b = \Omega_{\text{in}} R_{\text{in}}^2 \frac{1 - \mu}{1 - \eta^2} \quad (9)$$

with the ratios (5) and (6). The Rayleigh limit is defined by $a = 0$, i.e. $\mu = \eta^2$. A quasi-Keplerian flow results for $\mu = \eta^{1.5}$ while $\mu = \eta$ leads to a flow with quasi-uniform linear velocity U_ϕ .

From (7) follows

$$R\Omega^2 \frac{\partial \rho_0}{\partial z} + g \frac{\partial \rho_0}{\partial R} = 0 \quad (10)$$

if the rotation law is forced to be independent of z . One finds $\partial \rho_0 / \partial R = -\epsilon \partial \rho_0 / \partial z$ with the ratio $\epsilon = R\Omega^2 / g$ of centrifugal acceleration to the gravity. Only for small ϵ in rotating fluids the radius-dependence of ρ_0 can be neglected.

The Froude number $Fr = \Omega_{\text{in}} / N$ as the ratio between the rotation rate Ω_{in} of the

inner cylinder and the Brunt-Väisälä frequency

$$N = \sqrt{-g \frac{\partial \log \rho_0}{\partial z}} \quad (11)$$

describes a normalized rotation rate. The Reynolds number Re and the Brunt-Väisälä number Rn are defined by

$$Re = \frac{\Omega_{\text{in}} R_{\text{in}} D}{\nu}, \quad Rn = \frac{N R_{\text{in}} D}{\nu}, \quad (12)$$

hence $Fr = Re/Rn$. The gap width is $D = R_{\text{out}} - R_{\text{in}}$.

For the normalized centrifugal acceleration ϵ one finds $\epsilon \simeq Fr^2 Rg/c_{\text{ac}}^2$ with c_{ac} as the speed of sound which for water is more than 10^5 cm/s. Hence, Rg/c_{ac}^2 is $\mathcal{O}(10^{-6})$ for $R \simeq 10$ cm. The condition $\epsilon \ll 1$ is thus always fulfilled so that the centrifugal acceleration can be neglected in Eq. (10).

Consider the basic flow, density and pressure as perturbed to a flow $\mathbf{U} + \mathbf{u}$, density $\rho_0 + \rho$ and $P + p$. In cylindric geometry the Boussinesq form of the system of hydrodynamic equations for the perturbations \mathbf{u} and p is

$$\begin{aligned} \frac{\partial u_R}{\partial t} + \Omega \frac{\partial u_R}{\partial \phi} - 2\Omega u_\phi &= -\frac{\partial}{\partial R} \left(\frac{p}{\rho_0} \right) + \nu \left(\Delta u_R - \frac{2}{R^2} \frac{\partial u_\phi}{\partial \phi} - \frac{u_R}{R^2} \right), \\ \frac{\partial u_\phi}{\partial t} + \Omega \frac{\partial u_\phi}{\partial \phi} + \frac{1}{R} \frac{\partial R^2 \Omega}{\partial R} u_R &= -\frac{1}{R} \frac{\partial}{\partial \phi} \left(\frac{p}{\rho_0} \right) + \nu \left(\Delta u_\phi + \frac{2}{R^2} \frac{\partial u_R}{\partial \phi} - \frac{u_\phi}{R^2} \right), \\ \frac{\partial u_z}{\partial t} + \Omega \frac{\partial u_z}{\partial \phi} &= -\frac{\partial}{\partial z} \left(\frac{p}{\rho_0} \right) - g \frac{\rho}{\rho_0} + \nu \Delta u_z, \\ \frac{\partial}{\partial t} \left(\frac{\rho}{\rho_0} \right) + \Omega \frac{\partial}{\partial \phi} \left(\frac{\rho}{\rho_0} \right) - \frac{N^2}{g} u_z &= 0 \end{aligned} \quad (13)$$

with $\Delta F = \partial^2 F / \partial R^2 + (1/R) \partial F / \partial R + (1/R^2) \partial^2 F / \partial \phi^2 + \partial^2 F / \partial z^2$ and for incompressible fluids, $\text{div } \mathbf{u} = 0$. The ρ_0 in the system denotes a constant reference value of the density. The last equation in (13) describes the generation of density fluctuations by a flow field in combination with an axial gradient of the background density. The adiabatic temperature equation used in the presence of a prescribed temperature gradient has the identical form, see [10].

As we shall always consider the Brunt-Väisälä frequency N as uniform the coefficients of the system only depend on the radial coordinate, so that a normal mode expansion of the solutions,

$$F(R, \phi, z, t) = F(R) e^{i(m\phi + kz - \omega t)}, \quad (14)$$

can be applied with the azimuthal wave number m , the axial wave number k and the complex Fourier frequency ω for all fluctuating quantities. The no-slip boundary conditions at the inner and outer cylinder ($u_R = u_\phi = u_z = 0$) complete the eigenvalue problem. Note that there is no molecular density diffusion κ in the system hence the microscopic Prandtl number $Pr = \nu/\kappa$ is assumed as infinity. [20] work with a ratio of the diffusivities of 700 which certainly allows the adiabatic approximation (13). The Prandtl number of the silicon oil used in the apparatus shown in Fig. 1 is

57. The condition that in the last relation of (13) a molecular diffusion term can be neglected against the drift term of the nonaxisymmetric instability pattern simply reads $mRe > 1/Pr$ which is always fulfilled for Prandtl numbers exceeding unity.

A linear code is used to solve the set of ordinary differential equations for the radial profiles of flow, density and pressure. The solutions are optimized with respect to that axial wave number k which provides the lowest Reynolds number. The wave numbers are normalized with the characteristic radius $R_0 = \sqrt{R_{in}D}$ (which for $\eta = 0.52$ is very close to the gap width D) and the frequencies ω with the rotation rate Ω_{in} of the inner cylinder. As described by [25] the code has been tested with data of [33].

We shall start with the discussion of the conditions for neutral stability in the (Rn/Re) plane of the modes. Neutral instability implies vanishing growth rates. The shear number μ is considered as the free parameter.

4. Potential flow

The most prominent example for the instability is the potential flow with $\mu = 0.27$. [15] argue that the instability of the stratified potential flow is the most unstable one in agreement with our numerical results. Figure 4 shows the lines of marginal instability derived from (13) for vanishing imaginary part of ω . The potential flow proves to be unstable against nonaxisymmetric perturbations with low mode numbers m . The lines of neutral stability in the given sector are almost straight lines so that a necessary condition $Fr < Fr_{max}$ for instability of the potential flow against nonaxisymmetric perturbations is suggested with $Fr_{max} \simeq 5.5$ for $Re \lesssim 1000$. The values for the non-potential flows with weaker shear, however, will be basically smaller. Figure 8 shows that for $Re > 1000$ the values of Fr_{max} start to depend on the Reynolds number. The stability curves in the full (Rn/Re) planes are more complex to be described in terms of a single Fr .

The main result from Fig. 4 is that the instability domain forms a cone in the (Rn/Re) plane with an upper fast-rotation bound and a lower slow-rotation bound. The stability curves always possess a minimum Rn . For larger Rn there are always two Reynolds numbers Re limiting instability cone. The rotation can thus be too slow and it can be too fast for SRI. The difference between the maximum and the minimum Re increases for increasing Rn . For Re larger than its absolute minimum value the line $Fr = 1$ always belongs to the instability domain. Also no crossing points of the two lines of neutral instability have been found for the potential flow with the straight lines $Fr = 1$ or $Fr = 2$. The form of the instability curves suggests that this condition also holds for very large Reynolds numbers, i.e. in the diffusion-less limit $\nu \rightarrow 0$. We shall see below that this statement does not remain true if more flat rotation laws are considered.

Figure 4 also shows the instability maps of the modes with $m = 2$ and $m = 3$ which both are close to the curve for $m = 1$. The latter encloses the curve for $m = 2$ which itself encloses the curve for $m = 3$. For the upper branch in the (Rn/Re) plane

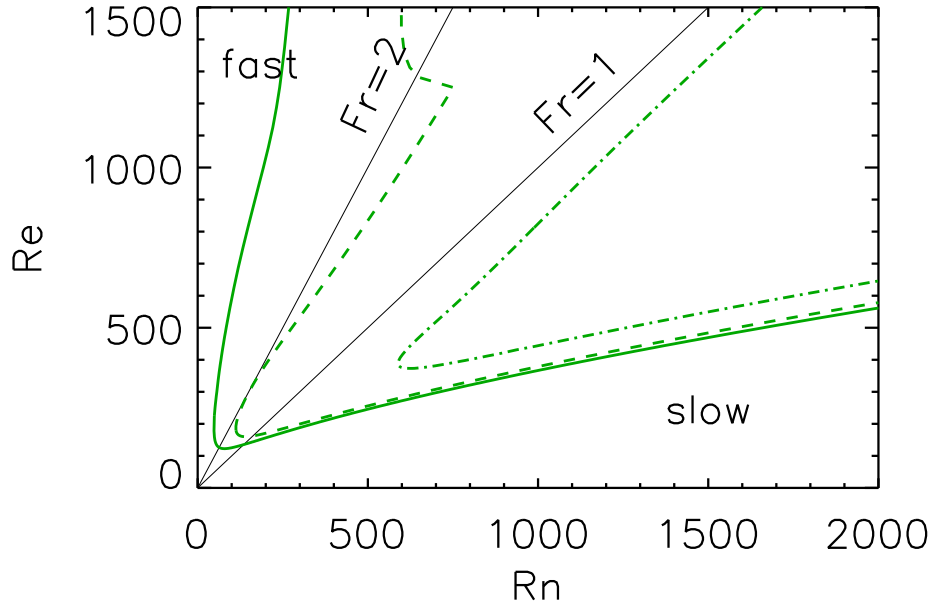


Figure 4. Stability map for the modes with $m = 1$ (solid), $m = 2$ (dashed) and $m = 3$ (dot-dashed) in the (Rn/Re) plane for the potential flow. The gray solid lines display $Fr = 1$ and $Fr = 2$. $\eta = 0.52$, $\mu = 0.27$.

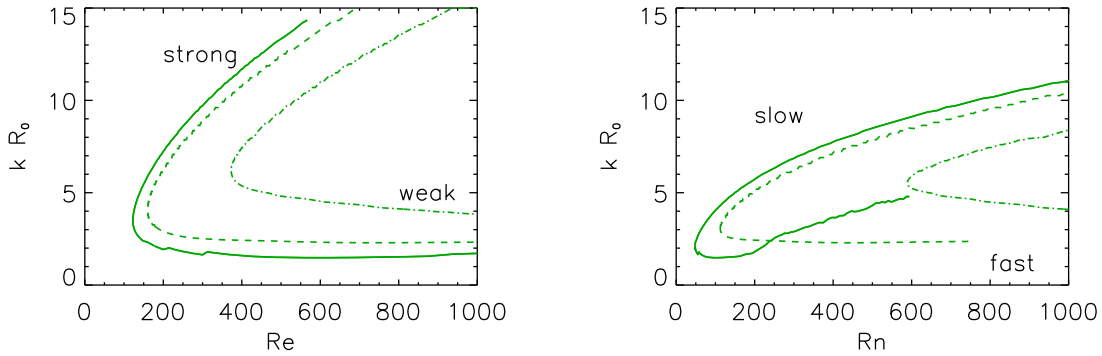


Figure 5. Axial wave numbers kR_0 along the lines of neutral instability shown in Fig. 4 for $m = 1, 2, 3$ as functions of Re (left) and Rn (right). The upper branches of the lines belong to strong stratification (left) and/or to slow rotation (right). Strong stratification and/or slow rotation lead to high wave numbers and vice versa. $\eta = 0.52$, $\mu = 0.27$.

representing the solutions for fast rotation the different lines are easy to see while they are much more close together at the lower branch. This means that strong shear has a stronger stabilizing effect to the modes with higher m than for $m = 1$. We shall see below that this mechanism is even more effective for flatter rotation laws.

In Fig. 5 the normalized axial wave numbers along the lines of neutral stability

are given for the modes $m = 1, 2, 3$ as a function of the Reynolds number (left) and of the Brunt-Väisälä number (right). The lower parts of the curves belong to the upper branches in the stability map while the upper parts in the two panels represent the lower branches in the instability map. For fixed Reynolds number weak stratification leads to small axial wave numbers and strong stratification leads to large wave numbers. The action of the Taylor-Proudman theorem can be recognized by the right panel of Fig. 5. For fixed stratification fast rotation produces small axial wave numbers and slow rotation produces large wave numbers. Note that at the beginning of the fast-rotation branch of the potential flow in Fig. 5 the wave numbers are almost constant with $kR_0 \simeq 2$.

The equation system (13) only possesses solutions for finite values of the Fourier frequency ω . Its imaginary part provides the growth or decay rate of the solution while its real part describes an azimuthal drift of the entire nonaxisymmetric instability pattern. It is here given by the real part ω_{dr} of the frequency ω of the Fourier expansion (14) normalized with the rotation rate of the inner cylinder. Because of

$$\frac{\dot{\phi}}{\Omega_{\text{in}}} = \frac{\omega_{\text{dr}}}{m\Omega_{\text{in}}} \quad (15)$$

the azimuthal drift has the same sign of ω_{dr} . As the drift rates in Fig. 6 (left panel) are always positive the patterns always migrate in positive ϕ -direction. Note that a drift value of μ describes exact corotation of the instability pattern with the outer cylinder. The positive deviation from this value makes the pattern slightly faster rotating than the outer cylinder.

The drift (15) for the potential flow (along the slow-rotation branch of the instability cone) almost proves to be independent of Rn . The numerical values only show a slight increase towards large Rn (Fig. 6, left). On the other hand, Fig. 6 (right) presents the values of (15) as function of μ for three models with a wide, a medium and a narrow gap. The lines demonstrate a linear relation of the azimuthal drift and the shear μ , i.e. $\dot{\phi}/\Omega_{\text{in}} = \alpha(\mu - \eta^2) + \eta$ which leads to $\dot{\phi}/\Omega_{\text{in}} = \eta$ for the potential flow with $\mu = \eta^2$. These drift values are indeed very close to the diamonds positioned at the dotted line. The coefficient α represents the slope between the normalized drift and the shear μ . To fix this slope we assume $\dot{\phi}/\Omega_{\text{in}} = 1$ for $\mu = 1$ from the right panel of Fig. 6 as valid for all η and find

$$\frac{\dot{\phi}}{\Omega_{\text{in}}} = \frac{\mu + \eta}{1 + \eta}. \quad (16)$$

For the container with $\eta = 0.52$ a slope of $\alpha = 0.66$ between drift and shear is expected. With respect to the rotation of the *outer* cylinder (16) leads to

$$\frac{\dot{\phi}}{\Omega_{\text{out}}} = \frac{1}{\mu} \frac{\mu + \eta}{1 + \eta}, \quad (17)$$

so that $\dot{\phi}/\Omega_{\text{out}} = 1/\eta$ for the potential flow. Hence, for very thin gaps with $\eta \rightarrow 1$ this yields $\dot{\phi} = \Omega_{\text{out}}$ hence instability pattern and outer cylinder are exactly corotating in this limit. For containers with finite gaps the pattern migrates slightly faster than the

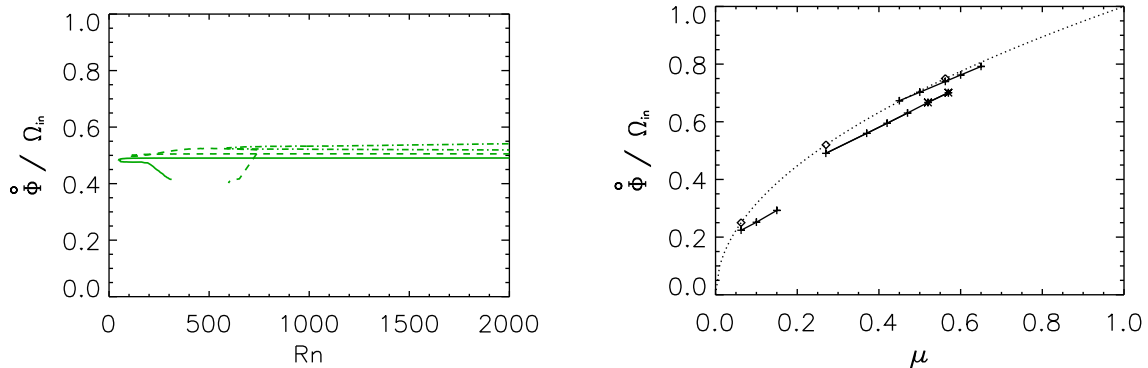


Figure 6. Left: Drift values (15) of the nonaxisymmetric modes with $m = 1, 2, 3$ (solid/dashed/dot-dashed) for the potential flow with $\eta = 0.52$ and $\mu = 0.27$. The data belong to the slow-rotation branches and to the fast-rotation branches in Fig. 4. Right: Drift values for $m = 1$ as function of the rotation ratio μ for three different gaps with $\eta = 0.25$, $\eta = 0.52$, $\eta = 0.75$ (from left to right). The dotted curve gives $\dot{\phi} / \Omega_{in} = \sqrt{\mu}$ for the potential flow of the three models.

outer cylinder rotates. The differences to the rotation of the outer cylinder are a proxy of the gap width. Formally, for $\mu \gg \eta$ the relation $\dot{\phi} \simeq \Omega_{out} / (1 + \eta)$ results independent of μ .

Empirical results from measurements with the SRI-container described in Section 2 can be used to measure the slope α . Figure 7 compares the heuristical formulation (16) with the empirical data. The drift rate linearly runs with the shear parameter μ . The more rigid the rotation the closer are the values of the observed pattern drift and the calculated results. Differences between the numerical results and the measurements mainly appear for the steepest rotation laws. The resulting observed slope is $\alpha \simeq 0.77$. Indeed, Fig. 6 (left) shows the drift of the potential flow with $\mu = \eta^2$ being slightly smaller than the approximation (16) predicts. It is however, not possible, to explain the deviations of the theoretical and the observed slope only with small inaccuracies of the applied assumptions as they appear in Fig. 6. The relation (16) concerns the horizontal lines in this plot for slow-rotation but the values for the fast-rotation lines do hardly differ. The drift rates are uniform in the entire instability cones of Fig. 4. For given rotation ratio μ the measurements shown in Fig. 7 fill the whole unstable interval.

In summary, the measured drift values are in good agreement with those derived from the linear stability analysis. Nonlinear simulations for models with endplates suggest that the deviations are produced by the two endplates which have been ignored in formulating the relation (16) but this unexpected result is beyond the scope of this paper.

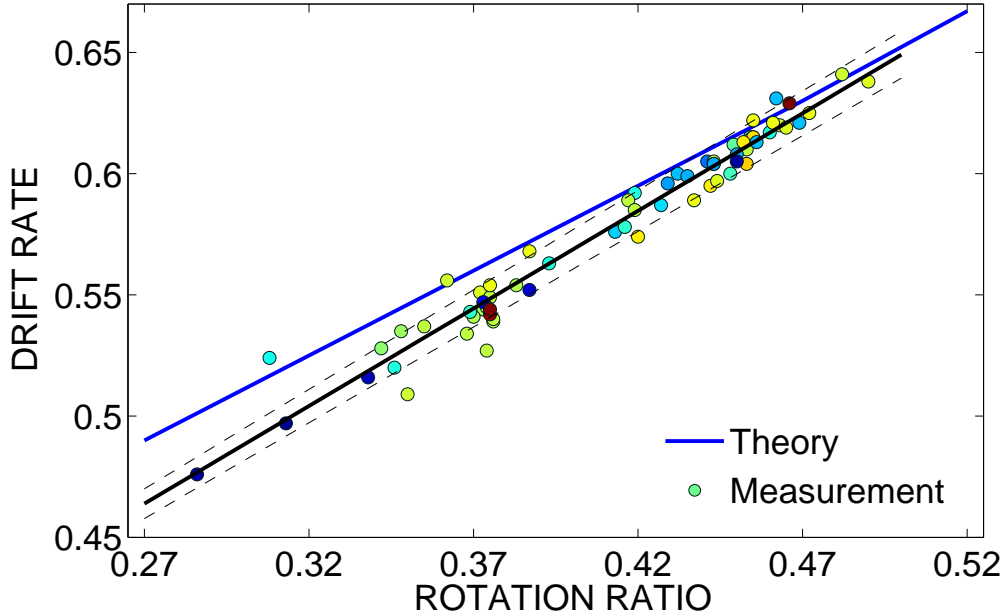


Figure 7. Azimuthal drift rates (15) in comparison with the experimental results for $Rn = 150 \pm 30$ (blue dots), $Rn = 210 \pm 30$ (light blue dots), $Rn = 270 \pm 30$ (green dots), $Rn = 330 \pm 30$ (yellow dots), $Rn = 390 \pm 30$ (brown dots). The solid blue line gives the linear relation (16). The slope of the dark solid line representing the measurements is 0.77; between the two dashed lines 95% of all measurements are located. The slope of the blue line is the same for all Rn intervals. The drift always exceeds the rotation ratio μ so that the instability patterns overturn the outer cylinder. $m = 1$.

5. Flat rotation laws

Figure 8 shows the lines of marginal instability for rotation laws beyond the Rayleigh line, $\mu = 0.27$. The curves are labeled with the shear parameter μ of the differential rotation. For $\eta = 0.52$ the quasi-Keplerian flow is represented by $\mu = 0.37$ and the quasi-uniform flow $U_\phi \simeq \text{const}$ by $\mu = 0.52$.

We find all rotation laws for $\mu \leq \mu_{\max}$ with $\mu_{\max} = 0.57$ to be unstable for moderate Reynolds numbers in the (Rn/Re) plane. The instability domain, however, continuously decreases for increasing μ . For fixed stratification always two Reynolds numbers exist between them the flow is unstable. In particular, the flow is stabilized by too fast rotation. This rotational stabilization is much stronger for the flat rotation laws than it is for the steeper profile of the potential flow. The transition from strong to weak stabilization lies somewhere between $\mu = 0.42$ and $\mu = 0.47$ where the curvature of the lines of neutral instability changes its sign. For $\mu > 0.52$ these lines encircle closed domains which always contain the line $Fr = 1$. The rotation profiles flatter than the rotation law of the quasi-uniform flow (where $\mu = \eta$) always possess even an upper Brunt-Väisälä number stabilizing the flow.

One finds two different forms of the lines of neutral stability for fixed μ . They are closed if the rotation law is flat and they are open for steep rotation laws. At μ_{\max} even

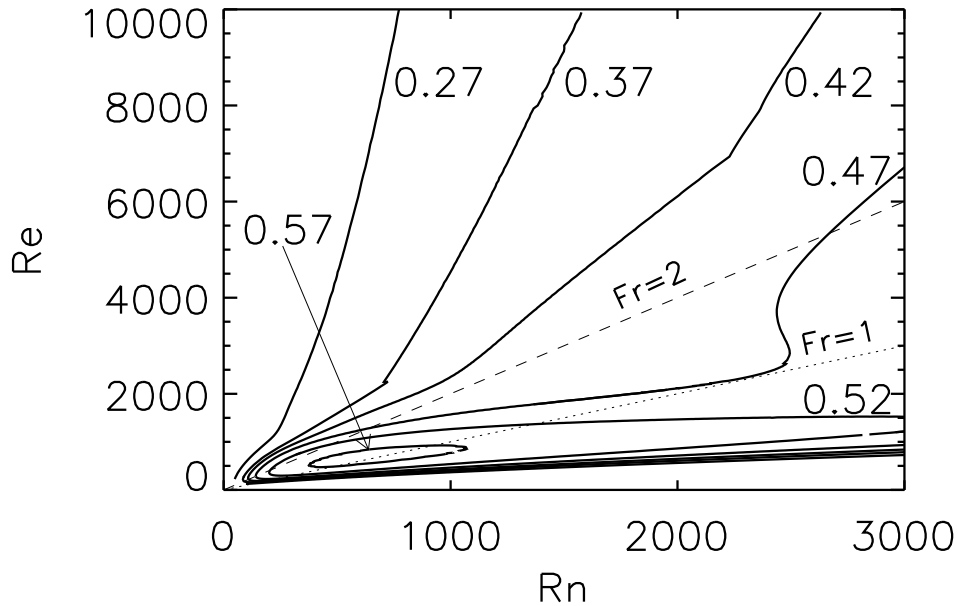


Figure 8. Stability maps of the $m = 1$ mode in the (Rn/Re) plane. The dotted (dashed) lines mark $Fr = 1$ ($Fr = 2$). The curves are marked with their shear value μ . The sign of the curvature of the lines for fast rotation depends on μ . The diffusive SRI disappears for $\mu_{\max} \simeq 0.57$ at $Re = Rn = 703$. $\eta = 0.52$.

the closed instability domain disappears. For $\mu > \mu_{\max}$ the SRI can thus only be excited for Reynolds numbers larger than (say) $\mathcal{O}(10^4)$. As an example, one finds $Re \simeq 60,000$ for instability of the rotation law with $\mu = 0.6$.

If the numerical results are mapped in the (μ/Re) plane then the stability lines for $Rn = \text{const}$ have the characteristic form shown in Figs. 9 and 10 which have already been observed by [13]. Different symbols represent the empirical results obtained in the experiment described in Section 2. The diamonds in Fig. 9 used for unstable flows demonstrate the existence of SRI for a wide range of shear values, Reynolds numbers and Brunt-Väisälä numbers. For given μ and Rn a lower Reynolds number and an upper Reynolds number exist. Theoretically, all flows with $Rn < 250$ (black rhombs) should only be unstable in region C which is indeed the case. The blue rhombs for flows with $250 < Rn < 375$ should not appear in the region A since the rotation is there too fast for the excitation of SRI. Probably because of endplate effects, the upper Reynolds number limit is not well-defined. For fast rotation the size of the pattern cells in axial direction would expand beyond the container height so that the system behaves no longer according to the linear equations of the axially unbounded system. On the other hand, the measurements precisely comply with the numerically found neutral line for slow rotation because of its rather large wave numbers.

The crosses in Fig. 10 mark experiments without indication of SRI. They define

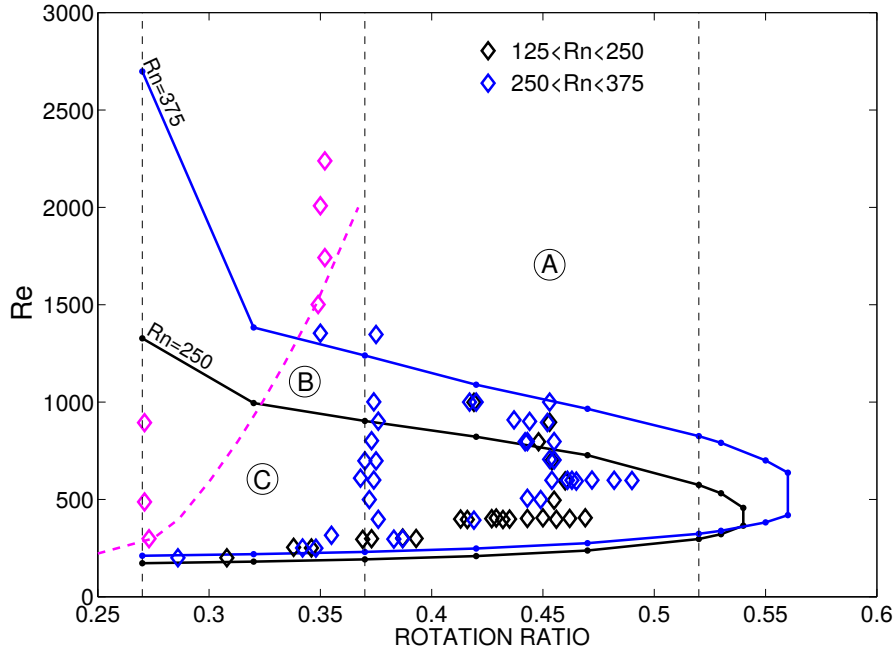


Figure 9. Calculated lines of neutral stability for the $m = 1$ mode in the (μ/Re) plane for $Rn = 250$ (black) and $Rn = 375$ (blue). The vertical lines stand for $\mu = 0.27$ (potential flow), for $\mu = 0.37$ (quasi-Keplerian flow) and $\mu = 0.52$ (quasi-uniform flow). The empirical results of the Cottbus SRI experiment are represented by diamonds as the symbol of instability. The pink line corresponds to the domain of strong endplate effects described in Fig. 3, also the measurements in this domain are marked by pink symbols. $\eta = 0.52$.

the domains of stability. Because of their definitions no black crosses should appear in region B and no crosses at all should appear in region C what is indeed the case. The curves of constant Rn are always crossing each other. Note that there is a turning point in the upper parts of the curves. The curves are concave for steep rotation laws and they are convex for flat rotation laws. Close to the Rayleigh line the stabilizing action of fast rotation is reduced.

The unstable rotation laws in the experiments fulfill $\mu \lesssim 0.49$. The island solutions for $\mu \gtrsim 0.50$ with their low growth rates have not been studied experimentally. The temperature differences of the used SRI experiment do not yet produce the needed high values of $Rn \simeq 700$.

6. Cell size and azimuthal drift

The axial size of a cell in units of the gap width D is

$$\frac{\delta z}{D} \simeq \frac{\pi}{k} \sqrt{\frac{R_{\text{in}}}{D}} \quad (18)$$

so that for $D \simeq R_{\text{in}}$ one finds $\delta z/D \simeq \pi/k$ with k as the wave numbers normalized with the radius R_0 . For large k the cells are oblate in axial direction. For $k \simeq \pi$ they

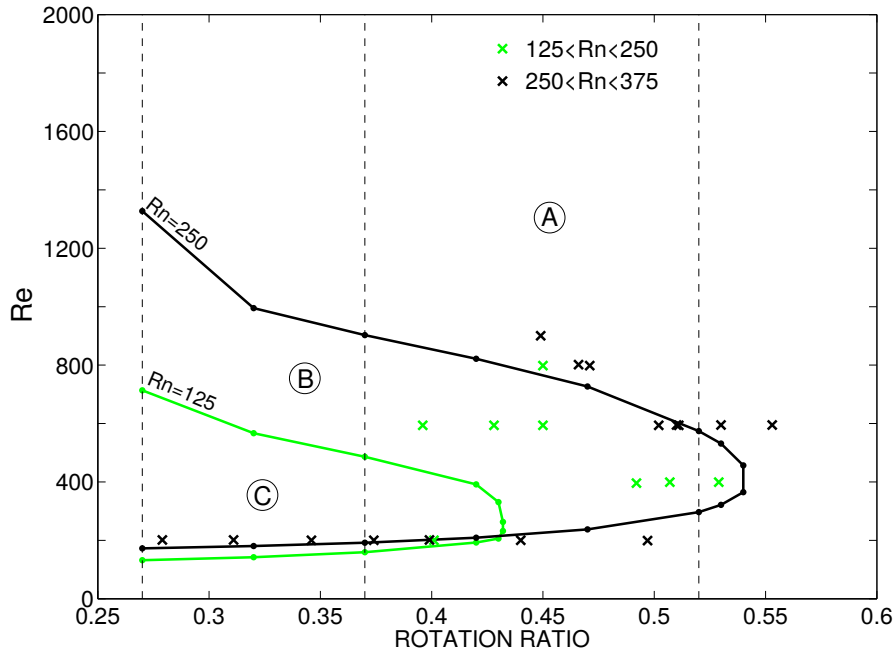


Figure 10. Same as in Fig. 9 but for the experiments leading to stable flows (crosses). Green line: neutral stability for $Rn = 125$, black line: neutral stability for $Rn = 250$.

are nearly circular. Figure 11 (left) gives the wave numbers along the lines of marginal stability. The green line compresses all wave numbers for the potential flow given in Fig. 5 for $m = 1$ in a surprisingly simple manner. $Fr > 0.5$ (fast rotation) leads to the fixed wave number $k \simeq 2$ while smaller Froude numbers (slow rotation) lead to $kFr \simeq 4$. For $k \simeq 2$ the relation (18) reads $\delta z/D \simeq 1.3$ leading to an axial cell size normalized with the size of the container, $\delta z/H \simeq 1.3/\Gamma$, which for $\Gamma = 10$ is certainly small enough even for experiments with fast rotation. For slow rotation the wave lengths are much shorter.

For the flows with weaker shear we find the wave numbers depending on Fr in the rather compact relation $kFr \simeq 4$ for all μ , which with (18) yields

$$\frac{\delta z}{D} \simeq \frac{\pi}{4} \frac{\Omega_{\text{in}}}{N} \quad (19)$$

[18]. In this formulation the action of the Taylor-Proudman theorem is easy to realize since for fast rotation the axial cell sizes are larger than for slow rotation. The positive Brunt-Väisälä frequency N acts opposite: the weaker the stratification the more oblong are the cells. The wavelengths are short for slow rotation and large stratification. Equation (19) can be read as

$$Fr = 1.28 \Gamma \frac{\delta z}{H} \quad (20)$$

relating the aspect ratio Γ of a finite-height container to the maximally reasonable Fr . Provided the minimal number of cells in the container is (only) two then for $\Gamma = 10$, the fastest possible rotation follows from $Fr \simeq 6.3$. With four cells required, $Fr \simeq 3.1$ gives the upper limit. For the fast-rotation branch of the potential flow no such limit exists.

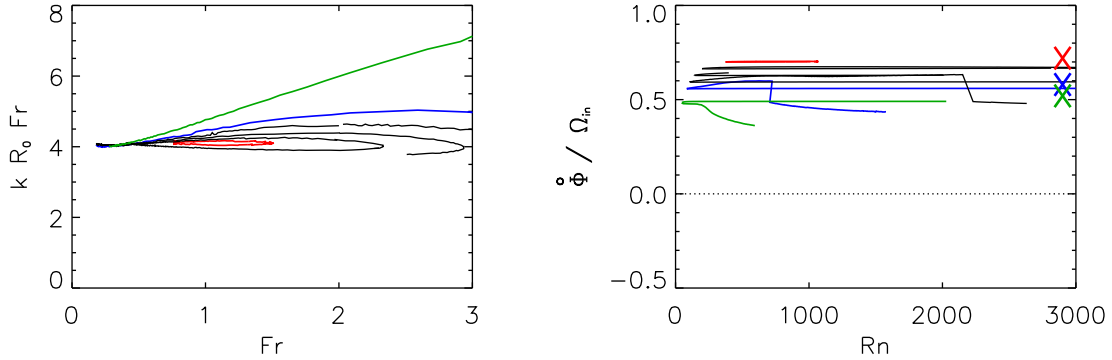


Figure 11. Left: Normalized axial wave numbers kFr along the lines of marginal stability for μ between 0.27 and 0.57 as a function of the Froude number Fr . Right: Drift rates (15). The crosses symbolize the numerical values provided by Eq. (16). Potential flow (green line), quasi-Keplerian flow (blue line), $\mu = 0.57$ (red line). $m = 1$, $\eta = 0.52$.

Again the drift rates of the patterns of marginal stability do not depend on the location in the (Rn/Re) plane. The weak dependence on the rotation law in Fig. 11 (right panel) approaches the linear run with μ in accordance to (16). The simplicity of these results is amazing. Along the lines of marginal stability the drift values (15) do not vary and the wave numbers are strictly anticorrelated to Fr with one and the same numerical factor with exception of the potential flow.

7. Growth rates

We briefly comment the growth rate ω_{gr} of the instability which is the imaginary part of the eigenfrequency normalized with Ω_{in} . The growth time τ_{gr} in units of the rotation time is $\tau_{gr}/\tau_{rot} = 1/(2\pi\omega_{gr})$. To find the characteristic growth rates of the instability of the quasi-Keplerian flow the frequencies are computed for a given Reynolds number with supercritical Rn . The Reynolds number is fixed to $Re = 2000$ for $\mu = 0.37$ (Fig. 12). One finds small values of order 0.01, i.e. the growth time is typically 6 turnovers of the *outer* cylinder. The maximal growth rates of the $m = 1$ mode appear for $Fr \lesssim 1$. This result, however, depends on the mode number m . The higher modes grow fastest for smaller Fr . It is thus possible that for larger Rn the growth rate of a higher mode exceeds that for a lower mode.

8. Summary and conclusions

In view of the laboratory experiment described in Section 2 the hydrodynamic equation system (13) has been solved numerically for the Taylor-Couette flow with the inner cylinder at $\eta = 0.52$ for various rotation laws. The potential flow gives the simplest example of the stratorotational instability. The lowest possible Reynolds numbers are

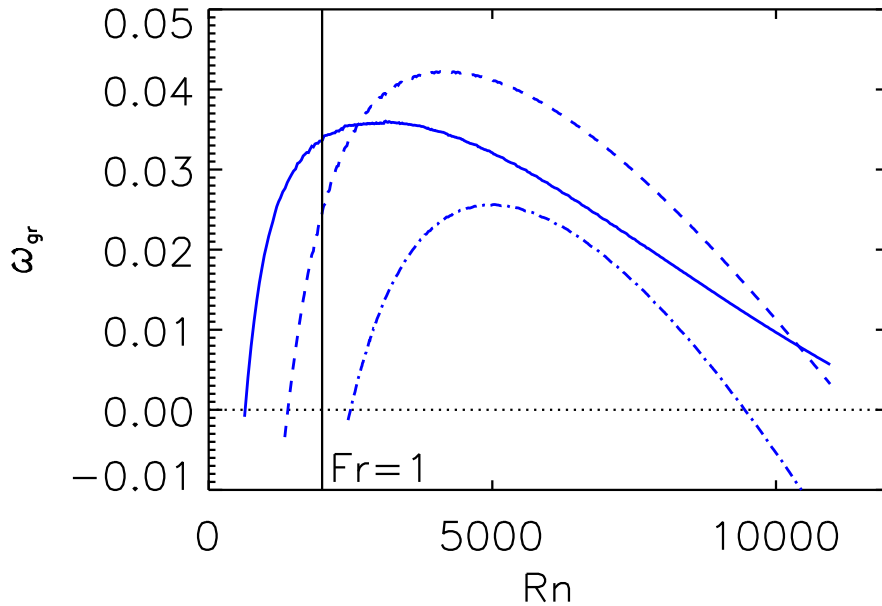


Figure 12. Growth rate ω_{gr} in units of Ω_{in} for quasi-Keplerian flow with supercritical Brunt-Väisälä number and fixed Reynolds number. $m = 1$ (solid), $m = 2$ (dashed), $m = 3$ (dot-dashed). The vertical line marks $Fr = 1$. $Re = 2000$, $\mu = 0.37$.

only 135 for the potential flow ($\mu = 0.27$) and $Re = 168$ for quasi-Keplerian flow ($\mu = 0.37$). There is a well-defined maximal value of $\mu = \mu_{\text{max}}$ at which the low- Re regime suddenly stops. The maximum μ_{max} increases for narrower gaps. For $\eta = 0.52$ the value of $\mu_{\text{max}} = 0.57$ indicates that the characteristic rotation law is slightly flatter than the quasi-uniform flow with $U_{\phi} \simeq \text{const}$. This finding remains true if the gap width is varied (Fig. 13).

Figure 8 presents the instability map for various shear values μ of the rotation laws between the cylinders. It shows the existence of a rotational stabilization of the SRI by fast rotation. The instability (for fixed Brunt-Väisälä number Rn) only exists between a low and a large Reynolds number. The rotational stabilization is stronger for lower Rn than for higher ones. The effect increases for increasing μ , i.e. for flatter rotation laws. For large μ the stability map even shows closed domains so that for these rotation laws not only a maximum Reynolds number exists but also a maximum Brunt-Väisälä number. Such instability islands only possess small Reynolds numbers with $\mathcal{O}(10^3)$. We also know that for very large Rn and flat rotation laws second instability areas occur in the map. For $\mu > \mu_{\text{max}}$ this instability type requires Reynolds numbers exceeding $\mathcal{O}(10^5)$ which, however, are not yet relevant for the present-day experimental possibilities.

Figures 9 and 10 show the theoretical instability domains for all $\mu < \mu_{\text{max}}$ for three Brunt-Väisälä numbers Rn . There is indeed always a lower Re and an upper Re limiting

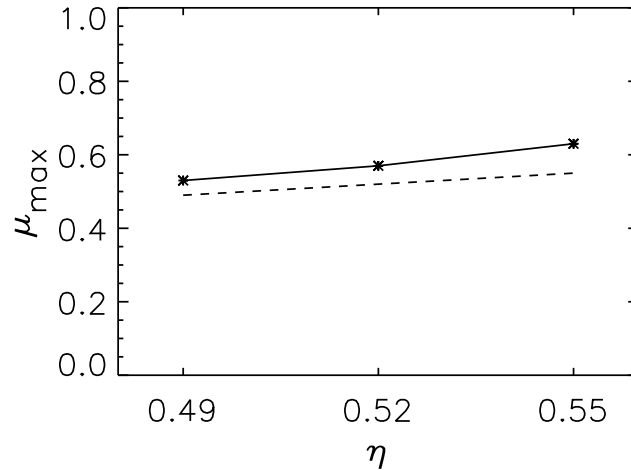


Figure 13. The theoretical maximal values of μ for various gap widths η . The dashed line denotes the rotation law with $\mu = \eta$. The calculated μ_{\max} represent rotation laws slightly flatter than $U_\phi = \text{const.}$

the instability area. The dependence of the lower limiting Re on Rn is very weak while it is much stronger for the upper limits. The experimental data added to the plots match these intervals with only a few exceptions at the fast-rotation branches. The low-rotation limit is almost perfectly confirmed by the measurements. The definition of the upper limit for fast rotation is less precise. There are, in particular, unstable flows with Kepler-like rotation laws for Reynolds numbers which should already lead to stability based on the numerical results. The wave numbers, however, at the upper line of neutral stability are so small that endplate effects by the apparatus (with aspect ratio $\Gamma = 10$) must be expected. Note that in Fig. 10 all crosses correctly indicate the expected stability for the flatter rotation laws.

Both azimuthal drifts and wave numbers of the nonaxisymmetric modes fulfill simple rules. The patterns always drift in the positive ϕ -direction – slightly faster than the outer cylinder rotates. Only for very narrow gaps ($\eta \rightarrow 1$) the instability pattern would precisely corotate with the outer cylinder. The pattern speed does neither depend on the Reynolds numbers nor on the azimuthal mode number m . The drift data from the Cottbus SRI experiment indeed demonstrate the rotation of the instability pattern as slightly faster than the rotation of the outer cylinder. The predicted linear relation between drift $\dot{\phi}$ and rotation ratio μ is also confirmed by the experiments. The theory describes the observed azimuthal drift phenomenon of the nonaxisymmetric perturbation patterns with acceptable accuracy (see Fig. 7).

One also finds a general rule for the wave numbers. Figure 11 provides $R_0 k$ for the modes with $m = 1$ in the regions of instability as basically behaving as $k \propto 1/Fr$. The cells are thus nearly circular in the (R/z) plane for $Fr \simeq 1$. They are prolate for fast rotation with $Fr > 1$ and they are oblate for slow rotation with $Fr < 1$. As an exception

the potential flow with $Fr > 1$ shows uniform values of the wave number independent of Fr . Nevertheless, to describe the shape of the instability cells is the true role of the Froude number in the theory of stratified Taylor-Couette flows.

References

- [1] ARLT, R. & URPIN, V. 2004 Simulations of vertical shear instability in accretion discs. *Astronomy & Astrophysics* **426**, 755–765.
- [2] AVILA, M. 2012 Stability and Angular-Momentum Transport of Fluid Flows between Corotating Cylinders. *Physical Review Letters* **108** (12), 124501.
- [3] AVILA, M., GRIMES, M., LOPEZ, J. M. & MARQUES, F. 2008 Global endwall effects on centrifugally stable flows. *Physics of Fluids* **20** (10), 104104–104104.
- [4] BOUBNOV, B. M., GLEDZER, E. B. & HOPFINGER, E. J. 1995 Stratified circular Couette flow: instability and flow regimes. *Journal of Fluid Mechanics* **292**, 333–358.
- [5] CATON, F., JANIAUD, B. & HOPFINGER, E. J. 2000 Stability and bifurcations in stratified Taylor Couette flow. *Journal of Fluid Mechanics* **419**, 93–124.
- [6] CHAGELISHVILI, G. D., ZAHN, J.-P., TEVZADZE, A. G. & LOMINADZE, J. G. 2003 On hydrodynamic shear turbulence in Keplerian disks: Via transient growth to bypass transition. *Astronomy & Astrophysics* **402**, 401–407.
- [7] DUBRULLE, B., MARIÉ, L., NORMAND, C., RICHARD, D., HERSANT, F. & ZAHN, J.-P. 2005 An hydrodynamic shear instability in stratified disks. *Astronomy & Astrophysics* **429**, 1–13.
- [8] ELSTNER, D., RÜDIGER, G. & TSCHÄPE, R. 1989 On the Schwarzschild criterion in accretion disk theory. *Geophysical and Astrophysical Fluid Dynamics* **48**, 235–249.
- [9] FRICKE, K. 1968 Instabilität stationärer Rotation in Sternen. *Zeitschrift f. Astrophysik* **68**, 317.
- [10] GELLERT, M. & RÜDIGER, G. 2009 Stratorotational instability in Taylor-Couette flow heated from above. *Journal of Fluid Mechanics* **623**, 375.
- [11] GOLDBREICH, P. & SCHUBERT, G. 1967 Differential Rotation in Stars. *The Astrophysical Journal* **150**, 571.
- [12] HUA, B. L., LE GENTIL, S. & ORLANDI, P. 1997 First transitions in circular Couette flow with axial stratification. *Physics of Fluids* **9**, 365–375.
- [13] IBANEZ, R., SWINNEY, H. L. & RODENBORN, B. 2016 Observations of the stratorotational instability in rotating concentric cylinders. *Physical Review Fluids* **1** (5), 053601.
- [14] LE BARS, M. & LE GAL, P. 2007 Experimental Analysis of the Stratorotational Instability in a Cylindrical Couette Flow. *Physical Review Letters* **99** (6), 064502.
- [15] LE DIZÈS, S. & RIEDINGER, X. 2010 The strato-rotational instability of Taylor-Couette and Keplerian flows. *Journal of Fluid Mechanics* **660**, 147–161.
- [16] LECLERCQ, C., PARTRIDGE, J. L., AUGIER, P., DALZIEL, S. B. & KERSWELL, R. R. 2016 Using stratification to mitigate end effects in quasi-Keplerian Taylor-Couette flow. *Journal of Fluid Mechanics* **791**, 608–630.
- [17] LIVIO, M. & SHAVIV, G. 1977 On the Stability of Accretion Disks. *Astronomy & Astrophysics* **55**, 95.
- [18] MOLEMAKER, M. J., MCWILLIAMS, J. C. & YAVNEH, I. 2001 Instability and Equilibration of Centrifugally Stable Stratified Taylor-Couette Flow. *Physical Review Letters* **86**, 5270–5273.
- [19] NELSON, R. P., GRESSEL, O. & UMURHAN, O. M. 2013 Linear and non-linear evolution of the vertical shear instability in accretion discs. *Month. Not. Roy. Astr. Soc.* **435**, 2610–2632.
- [20] PARK, J. & BILLANT, P. 2013 The stably stratified Taylor-Couette flow is always unstable except for solid-body rotation. *Journal of Fluid Mechanics* **725**, 262–280.
- [21] RICHARD, S., NELSON, R. P. & UMURHAN, O. M. 2016 Vortex formation in protoplanetary discs induced by the vertical shear instability. *Month. Not. Roy. Astr. Soc.* **456**, 3571–3584.

- [22] RÜDIGER, G., ARLT, R. & SHALYBKOV, D. 2002 Hydrodynamic stability in accretion disks under the combined influence of shear and density stratification. *Astronomy & Astrophysics* **391**, 781–787.
- [23] RÜDIGER, G. & SHALYBKOV, D. A. 2009 Stratorotational instability in MHD Taylor-Couette flows. *Astronomy & Astrophysics* **493**, 375–383.
- [24] SEELIG, T., BURCHARDT, M., KREBS, A., HARLANDER, U. & EGBERS, CH. 2016 PIV measurements in an axially stratified Taylor-Couette experiment. In *Lasermethoden in der Strömungsmesstechnik - 24. Fachtagung der GALA e.V.* (ed. Ch. Egbers, B. Ruck, A. Leder & D. Dopheide), p. 13.
- [25] SHALYBKOV, D. & RÜDIGER, G. 2005 Stability of density-stratified viscous Taylor-Couette flows. *Astronomy & Astrophysics* **438**, 411–417.
- [26] STOLL, M. H. R. & KLEY, W. 2014 Vertical shear instability in accretion disc models with radiation transport. *Astronomy & Astrophysics* **572**, A77.
- [27] SVEEN, J. K. 2004 An introduction to MatPIV v.1.6.1. *E-print series, Dept. of Math. University of Oslo, Mechanics and Applied Mathematics No.2*, ISSN 0809-4403.
- [28] TASSOUL, J.-L. 1978 *Theory of rotating stars*. Princeton: University Press.
- [29] TEVZADZE, A. G., CHAGELISHVILI, G. D. & ZAHN, J.-P. 2008 Hydrodynamic stability and mode coupling in Keplerian flows: local strato-rotational analysis. *Astronomy & Astrophysics* **478**, 9–15.
- [30] UMURHAN, O. M. 2006 On the stratorotational instability in the quasi-hydrostatic semigeostrophic limit*. *Month. Not. Roy. Astr. Soc.* **365**, 85–100.
- [31] URPIN, V. 2003 A comparison study of the vertical and magnetic shear instabilities in accretion discs. *Astronomy & Astrophysics* **404**, 397–403.
- [32] URPIN, V. & BRANDENBURG, A. 1998 Magnetic and vertical shear instabilities in accretion discs. *Month. Not. Roy. Astr. Soc.* **294**, 399.
- [33] WITHJACK, E. M. & CHEN, C. F. 1974 An experimental study of Couette instability of stratified fluids. *Journal of Fluid Mechanics* **66**, 725–737.
- [34] YAVNEH, I., MCWILLIAMS, J. C. & JEROEN MOLEMAKER, M. 2001 Non-axisymmetric instability of centrifugally stable stratified Taylor Couette flow. *Journal of Fluid Mechanics* **448**, 1–21.